

RESEARCH ARTICLE

10.1002/2016JC012581

The net energy budget at the ocean-atmosphere interface of the “Cold Tongue” region

Rachel T. Pinker¹ , Abderrahim Bentamy², Banglin Zhang¹ , Wen Chen¹, and Yingtao Ma¹

Key Points:

- Derived information on energy budget in climatic important region
- Evaluated quality of energy budget information against observations
- Provide guidelines for modelers for evaluation of their products

Correspondence to:

R. T. Pinker,
pinker@atmos.umd.edu

Citation:

Pinker, R. T., A. Bentamy, B. Zhang, W. Chen, and Y. Ma (2017), The net energy budget at the ocean-atmosphere interface of the “Cold Tongue” region, *J. Geophys. Res. Oceans*, 122, 5502–5521, doi:10.1002/2016JC012581.

Received 24 NOV 2016

Accepted 31 MAY 2017

Accepted article online 5 JUN 2017

Published online 10 JUL 2017

¹Department of Atmospheric and Oceanic Science, University of Maryland, College Park, Maryland, USA, ²Institut Français de Recherche pour l'Exploitation de la Mer, Plouzané, France

Abstract Pacific “Cold Tongue” (PCT) sea surface temperature (SST) experiences significant ($>0.5^{\circ}\text{C}$) interannual variations forced by the El-Niño Southern Oscillations (ENSO) with global impacts on the Earth climate. In this study, we estimate the PCT net heat budget known to be difficult to derive using numerical models. The main goal is to *determine how accurately the net heat flux across the surface/atmosphere interface can currently be determined* primarily, from satellite observations; these are first evaluated against the nearest available observations inside and outside the PCT of the Tropical Pacific Ocean, using buoy arrays such as the Tropical Atmosphere Ocean/Triangle Trans-Ocean Buoy Network (TAO/TRITON). It was found that the satellite-based estimates of both turbulent and radiative fluxes are in better agreement with the observations than similar estimates from leading numerical models. The monthly mean satellite estimates of PCT $\text{SW}\downarrow$ during January/July 2009 were 273.07/170.14, for $\text{LW}\downarrow$, latent heat and sensible heat they were 378.79/365.54, 95.52/130.31, 9.89/20.67, respectively (all in W/m^2). The estimated standard deviations for PCT $\text{SW}\downarrow$ were in the range of 7.2–7.8% of the mean and in the range of 2.0–2.5% for $\text{LW}\downarrow$, at daily time scale. Satellite estimates of both PCT LHF and SHF exhibit much higher variability, characterized by standard deviations of 50% from the mean values.

1. Introduction

1.1. Motivation

Large areas of surface cold water (also known as the “Cold Tongues”) are located westward from the continents along the equator in both the Atlantic and Pacific oceans, with persistent stratocumulus clouds. The Pacific feature is strongest in September/October, extending to the date-line, is weakest during March, and closer to the coast. The need to improve estimates of ocean heat fluxes has been recognized and articulated in numerous workshops as described in Yu *et al.* [2012, 2013], WCRP [2012], and CLIVAR/ESA Scientific Consultation Workshop and Programs [WCRP, 2013]. This led to the European Space Agency (ESA) Initiative to address key issues required for achieving these goals; they include a call for improvement in the retrievals of bulk variables such as surface winds, specific air humidity, air and surface temperatures, long time consistency of bulk variables over oceans, homogenization of Ocean Heat Flux (OHF) measurements used as “data reference,” OHF parameterizations for high and low winds, global long time series of OHF, validations and intercomparisons of available products at global and regional scales. Among the NASA Energy and Water cycle Study (NEWS) objectives included is the need to improve global closure of water and energy budgets by focusing on closure within specific regimes, such as the marine subsidence regions. This objective is also consistent with the European Space Agency (ESA) program to validate OHF products at regional scale, a first step before approaching the closure issue. The objective of the present study is to determine how well the heat flux across the air-sea interface can be determined, using currently available state-of-the-art observation, primarily, from satellites.

1.2. Background

The southern Tropical Pacific region of extensive low-level *stratocumulus clouds* is characterized by cold sea surface temperatures (SSTs) ($<26^{\circ}\text{C}$) in a narrow latitudinal band centered on the equator, primarily in the eastern part of the basin, and SSTs ($>27^{\circ}\text{C}$) in the western equatorial Pacific; it is also known as the Cold Tongue region. Our study will focus on a box bounded by (0–30°S, 110–70°W) as illustrated in Figure 1, considered in this study as the Cold Tongue. This region is of great interest in terms of understanding the atmosphere-ocean coupling, and the observed strong seasonal cycle in sea surface temperature (SST). As

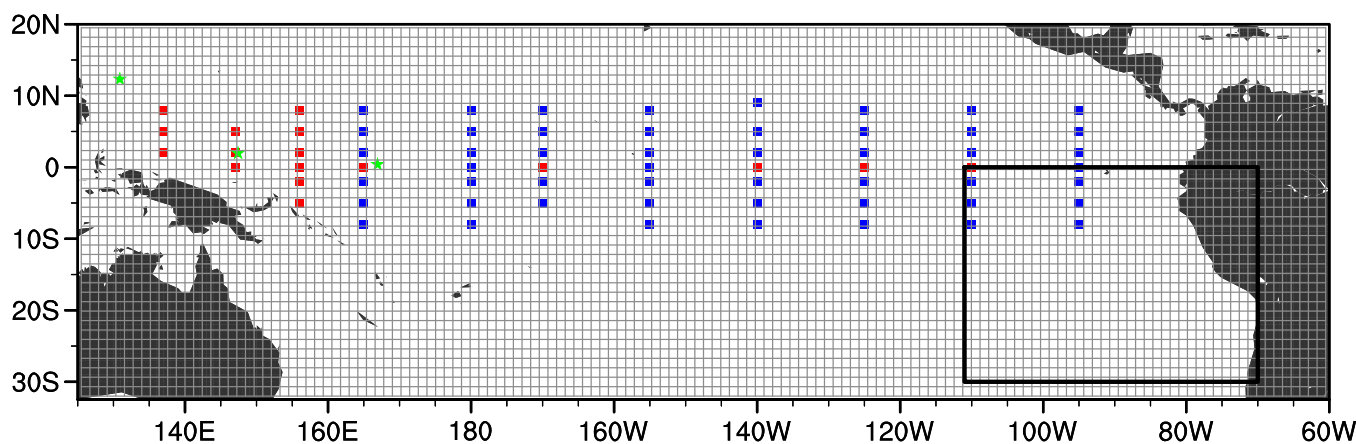


Figure 1. The squares represent the TAO/TRITON buoy locations; the red squares are the buoys we used in validation (17 sites). The green stars are the ARM/TWP sites (Nauru, Manus, Darwin). Only two sites (red) that have radiation measurements are in the Cold Tongue region.

noted previously [e.g., Zhang *et al.*, 2010; Klein and Hartmann, 1993], marine boundary layer (MBL) clouds that form over the cold water regions off the west coasts of major continents, impact radiative cloud forcing and play an important role in modulating the sea surface temperatures (SSTs). Available observations show that the amount of low-level marine clouds is highly correlated with lower-tropospheric stability (LTS) and cold air advection [Wood and Hartmann, 2006; Mochizuki *et al.*, 2007] and that surface-observed cloud fraction (CF) increases by 5.7% for each 1°K increase in LTS. Yet, the simulation of these clouds in global climate models (GCMs) is problematic [Siebesma *et al.*, 2004]. Some of these features have been investigated with numerical models while others used observations from oceanic arrays. Ma *et al.* [1994] used a coupled atmosphere-ocean general circulation model (CGCM) to examine the sensitivity of the simulated climate to the amount of Peruvian stratocumulus. The approach in their study was based on replacing the unrealistically low stratocumulus cloudiness produced by the model off Peru with constant overcast conditions. The enhanced stratocumulus resulted in a significant local cooling of the ocean surface *due to shielding from solar radiation*. Ma *et al.* [1994] found that the colder ocean surface underlying the stratocumulus region resulted in increased zonal and meridional SST gradients and enhanced Walker and Hadley circulations. Consistently, there was an increased surface evaporation and cooler SSTs immediately to the north of the region with artificially increased clouds. The work of Ma *et al.* [1994] was performed under highly idealized conditions. The constancy in time of the prescribed clouds, for example, precluded consideration of the potential effects of deviations from their annual mean; yet, such variations exist in nature and are significant. Klein and Hartmann [1993] showed that the area coverage of low-level clouds off the coast of Peru varies from about 40% in January to June to about 70% in July–December. The annual peak is in October when the atmospheric static stability is highest and the local SSTs are lowest.

Yu and Mechoso [1999] also hypothesized that the stratocumulus clouds play an important role in controlling the annual mean and annual variations of sea surface temperature (SST) in that region. They conducted sensitivity experiments in a region along the coast of Peru, using the University of California, Los Angeles, coupled atmosphere-ocean General Circulation Model (GCM) with different idealized temporal variations of stratocumulus. The surface sensible and latent heat flux and the *shortwave radiative flux* used for validation were those compiled by Oberhuber [1988] from observational data mainly from the Comprehensive Ocean-Atmosphere Datasets [Woodruff *et al.*, 1987] for the period 1950–1979. The zonal and meridional components of the surface wind stress were those analyzed at the Florida State University (FSU) by Legler and O'Brien [1985]. Among others, they examined the annual variations of the major components of the surface heat flux along the equator both in the observation, in the control run, and in the experiment. Their results show that *model errors in surface heat flux* at the equator over the eastern sector receive an important contribution from those in the *shortwave flux* component.

Swenson and Hansen [1999] used data from satellite-tracked drifting buoys and from the Voluntary Observing System Expendable Bathythermograph (VOS/XBT) profiles for the years 1979–1995 to evaluate how major oceanic processes redistribute heat in the Cold Tongue region of the tropical Pacific. The most active processes for the annual cycle are local heat storage and heat export by entrainment of upwelling and by

means of meridional advection. They report that heat export by zonal advection is not negligible, and meridional eddy heat fluxes associated with tropical instability waves have a negative feedback that offsets a considerable fraction of that produced by the mean meridional advection. All of these processes mimic the essentially 1 cycle/yr of the surface wind stress, as do those of the depths of both the bottom of the surface mixed layer and the thermocline. Due to the importance of the subject, numerous efforts are ongoing to address issues related to different aspects of the surface heat flux. For instance, *Josey et al.* [2013, 2014] have identified a pattern of unrealistic anomalies in near surface atmospheric humidity in the ERA-Interim [Dee et al., 2013] atmospheric reanalysis and derived data sets. They state that these anomalies have major consequence for air-sea heat exchange estimates. Associated annual mean heat flux anomalies centered on the mooring sites, as large as 30–50 W/m², are evident in the reanalysis derived data sets. The flux anomalies are problematic as these data sets are employed both to characterize ocean-atmosphere interaction and to force ocean models.

The budget equation for conservation of heat in the ocean surface mixed layer as used by *Swensen and Henson* [1999] is given as:

$$Q_0 - Q_h = \rho C_p \left\{ \frac{h D_H \Theta}{Dt} + \Delta T W_e \right\}$$

where Q_0 and Q_h are the downward heat flux across the top and bottom of the surface mixed layer, ρC_p is the heat capacity per unit volume of seawater, h is the mixed layer thickness, Θ is the vertically averaged temperature of the mixed layer, D_H/Dt is a horizontal operator, W_e is the entrainment or upwelling velocity at the bottom of the mixed layer, and ΔT is the difference between Θ and the scale coverage once their credibility has been established by comparison with high quality in situ data derived from buoys or dedicated platforms. For instance, the Tropical Atmosphere Ocean (TAO) array [McPhaden et al., 1998] provides data that can be used for the calibration and validation of remotely sensed data [Pinker et al., 2014]. Subsequently, the derived estimates of the Q_0 term and its components can be used to evaluate the net surface heat flux in ocean and climate temperature just below the mixed layer. For a closure of this budget there is a need for accurate estimates of each component. The objective of the present work is to assess the accuracy of Q_0 which is required for better characterizing the spatial and temporal patterns of the net heat budget over the *Cold Tongue* region. The focus of this study is to determine how accurately can the heat flux Q_0 across the top of the surface mixed layer be determined, using state-of-the-art observations, when possible, as derived from satellites. The advantage of satellite-based information is the ability to provide large scale information.

1.3. Outline of Work

Using satellite observations, we will derive the components of the heat budget in a region bounded by 0°–30°S, 110°W–70°W (Figure 1) (referred in this study as the *Cold Tongue*), and compare them to in situ measurements and to predictions from numerical models. The fluxes to be used are generated at daily and monthly time scales for a 10 year period (2002–2012) at a nominal 1° resolution (some parameters are derived at higher resolutions as will be noted). After obtaining metrics on the accuracy of the satellite estimates, they can subsequently serve as “ground reference” for evaluating numerical models. We will also compare time series of key parameters against similar observations at buoy sites that have the longest record for the period and the region of interest (sites at 95°W, 2°N and 110°W and 0° equator). Data used will be described in section 2, outline of result presentation will be given in section 3, results on validation will be presented in section 4, spatial variability of fluxes will be discussed in section 5, and discussion and summary will be given in section 6.

2. Data to be Used

Data used in the analysis are summarized in Table 1. Additional details will be provided in what follows.

2.1. Radiative Fluxes

Radiative fluxes, shortwave (SW↓), and longwave (LW↓) for the area of interest are from the following sources:

Table 1. Summary of Data Sources Used

Data Source	Type	Spatial Resolution	Temporal Resolution	Period Covered	Variables
IFREMER	Satellite	0.25° × 0.25°	Daily	1999–2009	LHF/SHF
SeaFlux	Satellite	0.25° × 0.25°	8 × daily	1998–2007	LHF/SHF
OAFIux	Blended	1.0° × 1.0°	Daily	1985–2014	LHF/SHF
ERA-I	Reanalysis	0.75° × 0.75°	6 hourly	1992–2012	LHF/SHF
CFSR	Reanalysis	0.38° × 0.38°	6 hourly	1992–2010	LHF/SHF
UMS/SRB DX		0.5° × 0.5°	3 hourly	1983–2012	SW and LW
UMD/SRB MODIS		1.0° × 1.0°	Daily	2002–2012	SW and LW

1. Based on observations provided under the International Satellite Cloud Climatology Project (ISCCP) [Rosenow and Schiffer, 1991] (this data version is known as DX and is sampled at pixel level) using an inference scheme developed at the University of Maryland (UMD_ISCCP_DX). The fluxes are derived globally and gridded to 0.5° at 3 hourly time scale from July 1983 to December 2009; they include both SW↓ [Ma and Pinker, 2012] and LW↓ [Nussbaumer and Pinker, 2012] flux components. For the period from January 2002 to December 2012, using an inference scheme labeled as UMD_MODIS_SW for SW↓ [Wang and Pinker, 2009] and UMD_MODIS_LW for LW↓ [Nussbaumer and Pinker, 2012], they are implemented globally with products from the Moderate Resolution Imaging Spectroradiometer (MODIS) sensor both on Aqua and Terra [King et al., 1992] at 1° spatial resolution at daily time scale (additional details on the ISCCP DX-based data are presented in Appendix A). Methodology how to homogenize the satellite estimates from the two independent sources, namely, ISCCP DX and Modis, is described in Appendix B.
2. ERA-Interim (ERA-I) [Berrisford et al., 2009; Dee et al., 2013] data as downloaded from <http://rda.ucar.edu>. Used are Monthly Mean Forecast Field (2/d) of Forecasts of 12 h Accumulation Gaussian Grid nLat*nLon = 256*512; units are W/m² s. Daily data are also from the Forecast Field Forecast Hours = 12 h Time Reference: 00UTC and 12UT, 2 records/d of 12 h Forecast Accumulation Gaussian Grid nLat*nLon = 256*512, in W/m² s.
3. The Climate Forecast System Reanalysis (CFSR) from the National Center for Environmental Prediction (NCEP) [Saha et al., 2010] as downloaded from <http://rda.ucar.edu/>. Monthly mean Forecast Field (4/d) of 6 h average Resolution 0.5° units: W/m²; Daily data Forecast Field-Forecast Hours = 6 h Time Reference: 00UTC, 06UTC, 12UTC, and 18UTC—4 records/d of 6 h Forecast Average Resolution 0.5°, units are W/m².
4. Buoy observations come from the Tropical Atmosphere Ocean/Triangle Trans-Ocean Buoy Network (TAO/TRITON) in the tropical Pacific Ocean [McPhaden et al., 1998]. Both radiative and turbulent fluxes are observed at the buoy sites. Only few of the buoys measure radiative fluxes as illustrated in Figure 1. For evaluation of radiative fluxes, we used data from buoys located at (0°, 110°W) and (0°, 125°W), the closest to the Cold Tongue box. To get a larger sample of observations, we used all buoy observations in the Tropical Pacific that were available for the period 2002–2009 and that measured radiative fluxes. The matching is done both in time and space. Selected are cases for which both satellite and ground observations are available at daily time scale. The spatial matching is based on the buoy location and the selection of the satellite grid box that covers that location. Subsequently, we evaluate the satellite value at the buoy location using weights that are function of lat/lon.
5. Observations of SW↓ and LW↓ fluxes at island stations are also utilized in this study since land-based observation are believed to be of higher quality than those from buoys. They represent tropical oceanic climate while allowing maintenance of the instruments according to the Baseline Surface Radiation Network (BSRN) guidelines [Ohmura et al., 1998]. Under the Department of Energy Atmospheric Radiation Measurement (ARM) Climate Research Program, three observational sites were established in the Tropical Western Pacific (TWP) and were operated by the Tropical Western Pacific Office (TWPO) at the Los Alamos National Laboratory (<https://www.arm.gov/sites/twp>). They include the Manus facility on Los Negros Island in Manus, Papua New Guinea (since 1996) (2°3′39.64″ S, 147°25′31.43″ E); the Nauru facility on Nauru Island, Republic of Nauru (since 1998) (0°31′15.6″ S, 166°54′57.60″ E); and the Darwin facility in Darwin, Northern Territory, Australia (since 2002) (12°25′28.56″ S, 130°53′29.75″ E). Covering the area roughly between 10°N and 10°S of the equator and from 130°E to 167°E, they include a region that plays a large role in the interannual variability observed in the global climate system. The Darwin facility operations and data collections officially ended on 31 December 2014. The Manus facility operations and data collections ended on 30 August 2014, and the Nauru facility operations and data collections ended on 30

August 2013. Issues related to accuracy of ground observations of radiative fluxes are discussed in Appendix C.

Information on buoy observations used for evaluation of turbulent fluxes is provided in the results section on turbulent fluxes. It needs to be noted that turbulent fluxes are not measured directly but rather are calculated from validated hourly buoy data of 10 m wind speed, specific air humidity, and air and sea surface temperature. The adjustment to 10 m height of basic variables (W_{10} , Q_a , T_a) and the estimation of turbulent fluxes are performed using COARE3 algorithm [Fairall et al., 2003]. Hourly validated buoy bulk variables and turbulent fluxes if available every day are daily averaged. The main criterion is: at least 6 hourly data should be available during day and night periods. For each day, daily buoy estimates are collocated in space with each flux product. The collocation criterion is the distance, separating buoy and flux product is less than the product spatial resolution.

2.2. Turbulent Fluxes

In Table 1, we summarize the characteristics of all the flux products used in this study (details on radiative fluxes are provided in section 2.1). Three types of estimated turbulent flux data, as available over global oceans, are considered. Estimates based only on remotely sensed observations such as those from IFREMER (Institut Français pour la Recherche et l'Exploitation de la MER), SeaFlux (Woods Hole Oceanographic Institution (WHOI)), or blended products known as OAFlex (Objectively Analyzed air-sea Flux (WHOI)). The third kind of flux products is derived from numerical weather predictions models. In this study, the reanalysis provided by the European Centre of Medium Weather Forecasts (ECMWF), ERA-I, and by the National Center for Environmental Prediction (NCEP), known as Climate Forecast System Reanalysis (CFSR), are used.

2.2.1. IFREMER

We use the new version of the IFREMER turbulent flux estimates over global oceans at daily time scale and at a spatial resolution of 0.25° longitude and latitude [Bentamy and Croize-Fillon, 2014]; it is an updated version of Bentamy et al. [2013]. The bulk variables such as surface wind speed (W_{10}) and specific air humidity (Q_{a10}) at 10 m height are estimated from remotely sensed observations. W_{10} is obtained from the SeaWind scatterometer on board QuikSCAT satellite. More specifically, this project uses new QuikSCAT wind retrievals known as QuikSCAT V3 as available from the Jet Propulsion Laboratory (JPL)/Physical Oceanography Distributed Active Archive Center (PODAAC) scientific team [Fore et al., 2014]. The new QuikSCAT V3 products are based on the use of a geophysical model function ensuring the consistency with winds retrieved from microwave radiometers such as the Special Sensor Microwave Imager (SSM/I) and WindSat [Ricciardulli and Wentz, 2011]. Wind retrievals are provided over QuikSCAT swath as Wind Vector Cell (WVC) of 12.5 km spatial resolution. This new scatterometer product is believed to improve wind speed estimate in rain and at high wind speed conditions.

Specific humidity is derived from the microwave imager (SSM/I) radiometer, based on a model relating brightness temperature measurements (T_b) and Q_{a10} [Bentamy et al., 2013]. SSM/I instruments are onboard the polar orbiting satellites DMSP F10, F11, F13, F14, and F15. For this project, a new processing of Q_{a10} is performed in conjunction with the use of the recently reprocessed fundamental climate data record (FCDR) of brightness temperatures from the Colorado State University [Sapiano et al., 2012; Kummerow et al., 2013].

Air and sea surface temperatures required for flux calculation are derived from ERA-I reanalyses (www.ecmwf.int/en/research/climate-reanalysis/era-interim) and from the Reynolds Optimally Interpolated version 2 (named hereafter NOAA SST) (<http://www.ncdc.noaa.gov/sst/>), respectively. Daily calculations of turbulent fluxes including wind stress and components, latent and sensible heat fluxes over global ocean at 0.25° spatial resolution are based on the updated bulk parameterization COARE3 [Fairall et al., 2003] as described in Bentamy et al. [2013].

2.2.2. SeaFlux

The SeaFlux product is available over global ice free oceans at 0.25° spatial resolution and at 3 hourly intervals (averaged from 0000 to 0300Z, 0300 to 0600Z, 0600 to 0900Z, etc.). Data are available from January 1998 to December 2007. Briefly, latent and sensible heat fluxes are estimated based on the use of COARE3.0 bulk parameterization [Fairall et al., 2003]. The required wind speed is derived from Cross-Calibrated Multi-Platform (CCMP) Ocean Surface Wind Components data [Atlas et al., 2011]. CCMP wind product at 10 m is calculated from cross-calibration and assimilation of wind retrievals from SSM/I, TMI, AMSR-E, QuikSCAT, and SeaWinds onboard ADEOS-2. Variational analysis method (VAM) is used for CCMP wind calculation over

global oceans. To start VAM, ECMWF reanalysis (ERA-40) is used for the period July 1987–December 1998; The ECMWF operational analysis is used from January 1999 to June 2009. CCMP data are available at synoptic times (00 h: 00, 06 h: 00, 12 h: 00, 18 h: 00 UTC) with a spatial resolution of 0.25° . The specific air humidity at 10 m and air temperature (T_a) are both retrieved using a method described in [Roberts *et al.*, 2010]. The method leads to the estimation of Q_{a10} and T_a based on the use of nonlinear regression algorithm (neural network) with microwave brightness temperatures. The algorithm requires SST information aimed at regularization of the inverse problem. SST required for SeaFlux calculation is the NOAA SST. Details on data and methods used can be found in Clayson *et al.* [2013], or at a dedicated website (<http://seaflex.org>).

2.2.3. OAFlex

The OAFlex estimates used in this study are available for years 1985–2014 at daily time scale and 1° spatial resolution [Yu *et al.*, 2008]. OAFlex estimates use NOAA SST daily values [Reynolds *et al.*, 2007] at a 0.25° horizontal resolution, SST values from the ECMWF reanalysis (ERA-40) and from the NCEP/CFSR and AMSR-E data. The SST data from the reanalyses are regridded by WHOI to 1° resolution to allow synthesis with the Reynolds SST data through objective analysis (used for all surface meteorological variables and fluxes); this analysis is based on the Gauss-Markov approach [Yu *et al.*, 2008]. For Q_{a2} estimation, OAFlex applies the Chou *et al.* [1995, 1997] algorithm. OAFlex approach also uses values at 2 m level from the NCEP and ECMWF reanalyses for specific humidity and applies advanced objective analysis to the inputs. For wind speed, OAFlex uses QuikSCAT and version 6 of the Special Sensor Microwave/Imager (SSM/I) data as described in Wentz [1997]. The data used for OAFlex calculations are 12 hourly averaged at a swath resolution of 25 km. Wind speeds are flagged if cloud/rain liquid water values exceeded 18 mg cm^{-1} because the accuracy of wind speed retrievals degrades in the presence of rain. Wind speed values are also flagged if measurements are within 50–100 km of the coast or within 200 km of the climatological monthly mean position of an ice edge. A variational method is applied to the data, which is subjective due to the determination of weights. The estimated winds are converted to the equivalent wind speed at 10 m height and to neutral stratification. Air temperatures are from NCEP and ECMWF reanalyses at 2 m height and advanced objective analysis is applied to the data; the analysis of air temperature is processed from 1 September 2002 and onward using the ERA-I reanalysis to replace NCEP. OAFlex turbulent fluxes are calculated based on the use of COARE3 parameterization.

2.2.4. ERA Interim (ERA-I)

ERA-I [Dee *et al.*, 2011] refers to the reanalyses of atmospheric parameters produced by the European Center for Medium Weather Forecasts (ECMWF). It uses 4D-variational analysis on a spectral grid. This reanalysis covers the period from 1989 to present. The ERA-I data used in this study were obtained from the ECMWF data server (http://apps.ecmwf.int/datasets/data/interim_full_daily/).

2.2.5. CFSR

NCEP Climate Forecast System Reanalysis (CFSR) (<http://rda.ucar.edu/pub/cfsr.html>) was developed by NOAA/NCEP. The data used in this study are from the NOAA's National Operational Model Archive and Distribution System (NOMADS), which is maintained by NOAA's National Climatic Data Center (NCDC) [Saha *et al.*, 2010]. The atmosphere and ocean models are coupled with no flux adjustment. Details on CFSR data are available at <http://cfs.ncep.noaa.gov/cfsr/>.

3. Roadmap to Result Presentation

Results from this study will be presented as follows:

1. Satellite-based and model-based estimates of radiative fluxes will be evaluated against buoy and island observations (sections 4.1 and 4.2).
2. Satellite-based and model-based estimates of turbulent fluxes will be evaluated against buoy observations (section 4.3).
3. Examples on the spatial distribution of radiative fluxes (SW_{\downarrow} , LW_{\downarrow} , and net) using a product that was compared favorably against observations over the domain of interest will be presented and discussed in section 5.1.
4. Examples on the spatial distribution of turbulent fluxes (LHF and SHF) over the domain of interest (using products that were evaluated against ground observations) and the spatial distribution of the net total flux (radiative and turbulent) will be presented and discussed in section 5.2.

5. Interannual variability and mean annual cycle of all the fluxes at two selected locations (where long records of observations were available) will be discussed in section 5.3.

4. Results

4.1. Evaluation of SW_↓ Fluxes

In Figure 2, we show results of evaluation for daily downward SW_↓ fluxes against two TAO buoy sites (0°N, 110°W and 0°N, 125°W) (Figure 1) for: (a) UMD_ISCCP_DX (2006–2009); (b) UMD_MODIS (2006–2009); (c) ERA-I (2000–2009); and (d) NOAA/CFSR (2000–2009). From the comparison of the two UMD products, it is seen that the MODIS results are closer to the buoy observations with a *bias* of -1.03 W/m^2 and *rms* of 19.00 W/m^2 which are only 0.4% and 6.8% of the mean, respectively. The ISCCP_DX results have a *bias* of -4.73 W/m^2 and *rms* of about 20.58 W/m^2 which are 1.7% and 7.4% of the mean, respectively, and have correlations in the range of 0.82–0.84. As evident, the satellite products are in better agreement with the buoys than CFSR, but they are not significantly better than ERA-I. A summary of all these results, for both daily and monthly time scales, is presented in Table 2. As evident, on monthly time scale, both *bias* and *std* are significantly reduced.

The evaluation of SW_↓ fluxes at monthly time scale was extended to 17 buoy sites, most of them, outside the area of interest. Specifically, the following products were used: (a) UMD_ISCCP_DX (2000–2009); (b) UMD_MODIS SW (2002–2009); (c) ERA-I (2000–2009); and (d) NOAA/CFSR (2000–2009). A summary of the

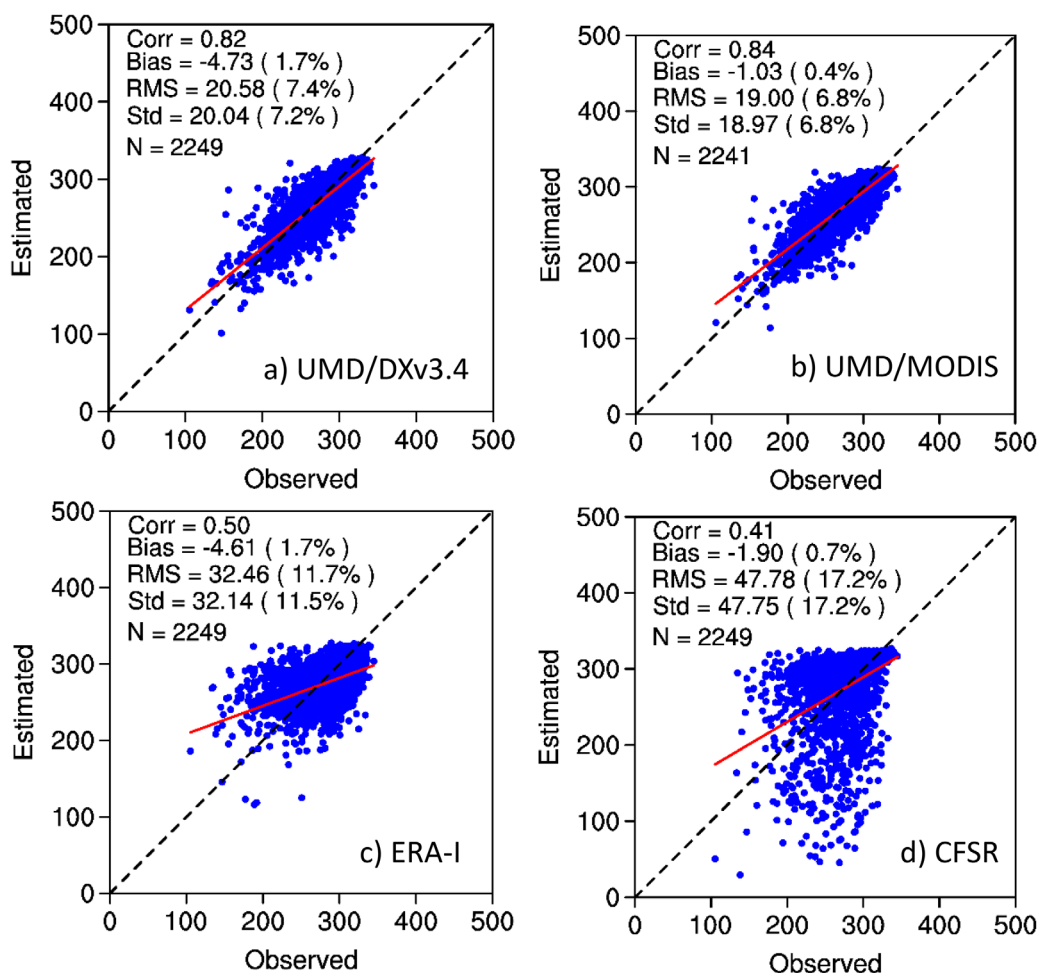


Figure 2. Evaluation of daily SW_↓ fluxes against two TAO buoy sites (0°N, 110°W and 0°N, 125°W) for (a) UMD_ISCCP_DX (2006–2009), (b) UMD_MODIS (2006–2009), (c) ERA-I (2006–2009), and (d) NOAA/CFSR (2006–2009). Numbers in parentheses indicate % of the mean (2006–2009) SW_↓ flux. Results at monthly time scale for the years (2002–2009) are summarized in Table 2.

Table 2. Evaluation Results of Daily and Monthly SW↓ Fluxes Against Two TAO Buoy Sites (0°N, 110°W and 0°N, 125°W) for: (a) UMD_ISCCP_DX (2006–2009), (b) UMD_MODIS (2006–2009), (c) ERA-I (2006–2009), and (d) NOAA/CFSR (2006–2009)

2 buoys Model	Daily						Monthly					
	SW↓			LW↓			SW↓			LW↓		
	cor	std	bias	cor	std	bias	cor	std	bias	cor	std	bias
UMD/DX	0.82	20.0	−4.7				0.81	8.5	−1.1			
UMD/MODIS	0.84	18.9	−1.0	0.87	8.1	−0.63	0.92	7.1	0.5	0.97	5.46	1.13
CFSR	0.41	47.8	−1.9	0.90	10.4	−4.2	0.76	15.4	−0.7	0.98	4.26	−4.26
ERA-I	0.50	32.1	−4.6	0.80	9.9	−1.5	0.75	11.8	−4.1	0.99	5.44	0.08

results for monthly SW↓ fluxes for the 17 sites are presented in Table 3. As seen, the ISCCP_DX results had a *bias* of -2.0 W/m^2 and *rms* of 13.1 which are about 0.9% and 6.0% of the mean, respectively, while the corresponding values for MODIS were -5.2 and 12.5 W/m^2 which are about 2.2% and 5.0% of the mean, respectively. The correlation for both was high, at about 0.94. As evident from above results, the selection of ground truth sites, associated with specific oceanic and atmospheric conditions, and the length of the evaluation period have an impact on the results. At issue are several factors. The primary one being that the quality of the buoy observations may vary from one site to the other.

Figure 3 shows results of evaluation of UMD_ISCCP_DX and UMD_MODIS for daily (2006–2009) time scales of SW↓ fluxes at three tropical Western Pacific (TWP) sites independently for each (sites are described in section 2.1(5)). Of interest is to note that island sites have an impact on the local conditions as documented for the Naura site by Long and McFarlane [2012] and as such, may impact the evaluation results of satellite data. This occurs primarily under convectively suppressed conditions such as La Nina as documented in McFarlane et al. [2005]. Basically there is a strong ENSO influence on Nauru, negligible for Manus, and Darwin [Riihimaki and Long, 2014]. In terms of *bias*, the performance of the UMD_DX product seems to do better than the MODIS product, while the *std* is similar.

Results at daily and monthly time scale for SW↓ fluxes at the TWP sites for the years (2002–2009), for each site independently and combined, are summarized in Table 4. As seen, both satellite products used in the evaluation perform similarly at these sites; however, the biases are higher than those for the MODIS products when evaluated against the TAO buoys. Possibly, this is due to the fact that the satellite footprint covers mixed land/ocean areas as well as issues related to island orography, which are known to be problematic in the evaluation of satellite retrievals against ground observations.

4.2. Evaluation of LW↓ Fluxes

The number of observing sites that measure LW↓ fluxes is much smaller than those that observe SW↓ fluxes; measurement of LW↓ fluxes is also more complex than for SW↓. Only two buoy sites, one at the north-western tip of the Cold Tongue region (0°N, 110°W), and the other at 0°N, 125°W were available and results at daily time scale for (a) UMD/MODIS, (b) ERA-I, and (c) CFSR are shown in Figure 4. This figure also includes results for the combined three TWP sites as shown in Figure 4d. Statistical results dealing with the evaluation of daily and monthly downward LW↓ fluxes from these cases (for the periods specified in Figure 4

Table 3. Evaluation Results of Monthly SW↓ Fluxes Against 17^a TAO Buoy Sites for: (a) UMD_ISCCP_DX (2006–2009), (b) UMD_MODIS (2006–2009), (c) ERA-I (2000–2009), and (d) NOAA/CFSR (2000–2009)

17 buoys	Monthly SW↓		
	cor	std	Bias
UMD/DX	0.93	13.1	−0.20
UMD/MODIS	0.94	12.5	−5.0
CFSR	0.71	25.4	37.8
ERA-I	0.92	13.6	−4.2

^a17 TAO sites (0°N, 110°W; 0°N, 125°W; 0°N, 140°W; 0°N, 147°E; 0°N, 156°E; 0°N, 165°E; 0°N, 170°W; 2°N, 137°E; 2°N, 147°E; 2°N, 156°E; 2°S, 156°E; 5°N, 137°E; 5°N, 147°E; 5°N, 156°E; 5°S, 156°E; 8°N, 137°E; 8°N, 156°E).

legends) are summarized in Table 2. As evident, on both time scales, the results in terms of *bias* and *std* are better than for the SW↓ fluxes, possibly, due to the fact that in the tropics, the water vapor is an important factor in determining the magnitude of the LW↓ flux; it is less variable in space in the tropics than clouds which affect the SW↓.

4.3. Evaluation of Turbulent Fluxes

The primary source of information on turbulent fluxes used in this study is

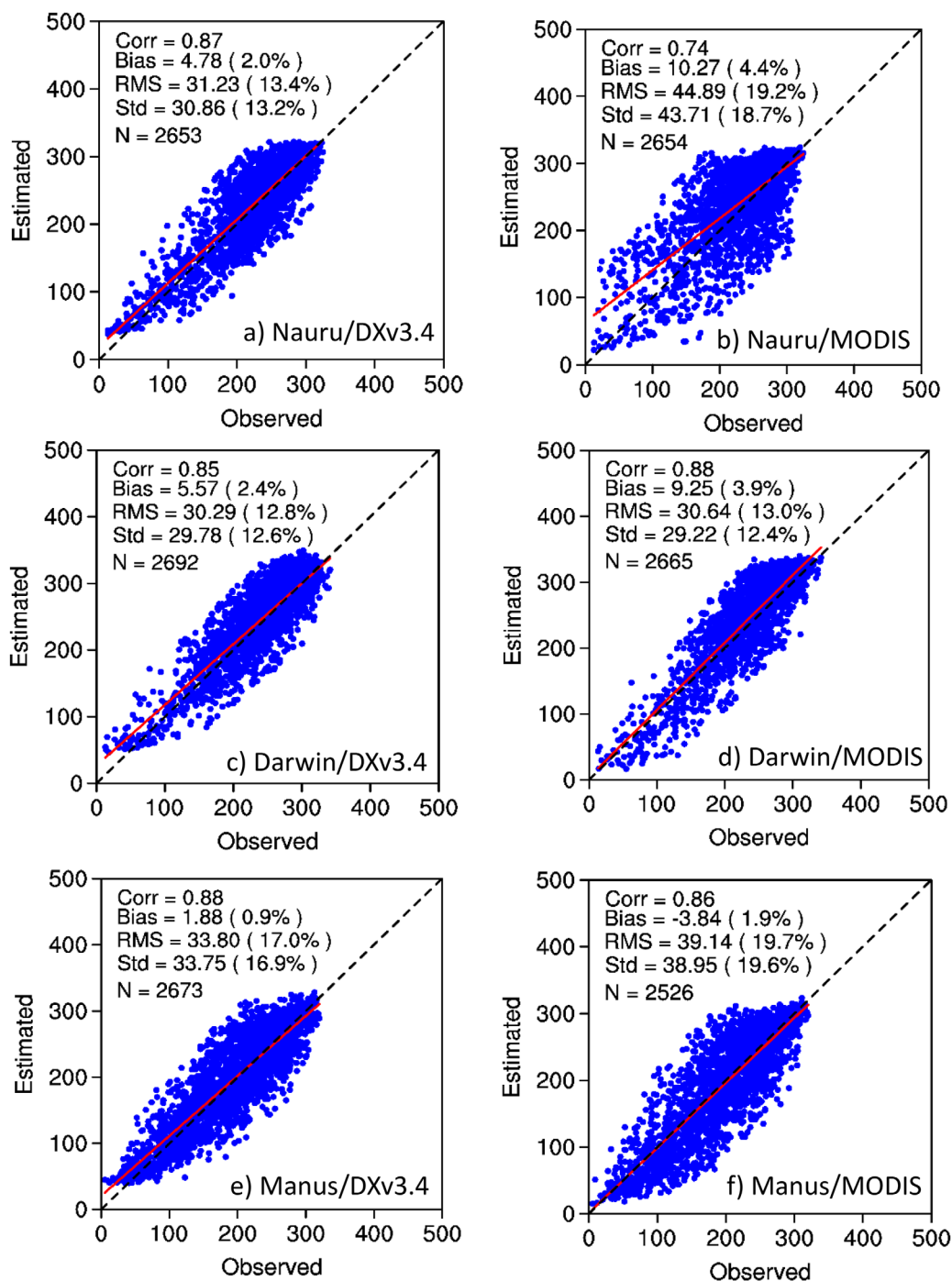


Figure 3. Evaluation of daily (2002–2009) mean downward SW fluxes from: (left) UMD_ISCCP_DX; (right) from UMD_MODIS at three Tropical Western Pacific (TWP) sites (independently): (a) Manus, Papua New Guinea: 2°3′39.64″S, 147°25′31.43″E; Nauru Island: 0°31′15.6″S, 166°54′57.60″E; and Darwin, Australia: 12°25′28.56″S, 130°53′29.75″E.

the IFREMER product. The quality of the daily latent (LHF) and sensible heat (SHF) fluxes is evaluated in this study by a comprehensive comparisons with buoys from 17 TAO/TRITON array available over the oceanic basin (8°S–12°N, 125°W–95°W). The buoy fluxes are not measured directly, but rather, determined from hourly buoy data, available at heights of 3.8 m. Buoy wind speeds, specific air humidity, and air temperature are converted to values at 10 m height using the COARE3.0 model [Fairall et al., 2003]. Daily fluxes as well as bulk variables (wind, sea surface temperature, specific air and surface humidity, air and sea temperatures)

Table 4. Assessment of Daily and Monthly Averaged SW_d Radiative Fluxes Against Observations Located Between 120° and 80°W, South of 2°N for 2000–2009 (DOE/ARM Climate Research Program Sites in the Tropical Western Pacific)

Site	Model	Daily SW _d			Monthly SW _d		
		cor	std	bias	cor	std	bias
Nauru	UMD/DX	0.87	30.9	4.8	0.95	12.0	6.0
	UMD/MODIS	0.74	43.7	10.3	0.94	12.5	9.8
Darwin	UMD/DX	0.85	29.8	5.6	0.93	14.2	6.32
	UMD/MODIS	0.88	29.2	9.3	0.96	13.1	9.3
Manus	UMD/DX	0.88	33.7	1.9	0.89	11.1	2.84
	UMD/MODIS	0.86	38.9	-3.8	0.89	11.7	-2.9
3 TWP	UMD/DX	0.87	33.2	5.8	0.94	12.5	5.1
	UMD/MODIS	0.84	38.2	5.6	0.96	13.7	5.4

are calculated from hourly measurements as arithmetic means. To place these results in the context of other available products, similar investigations are also performed for SeaFlux, OAFflux, ERA-I, and CFSR flux estimates. The resulting daily buoy data are collocated in space with each flux product. The collocation criterion is based on the distance separating buoys from the evaluated products; it has to be less than the product spatial grid characteristic. Statistics from the daily comparison between buoy and model estimates of

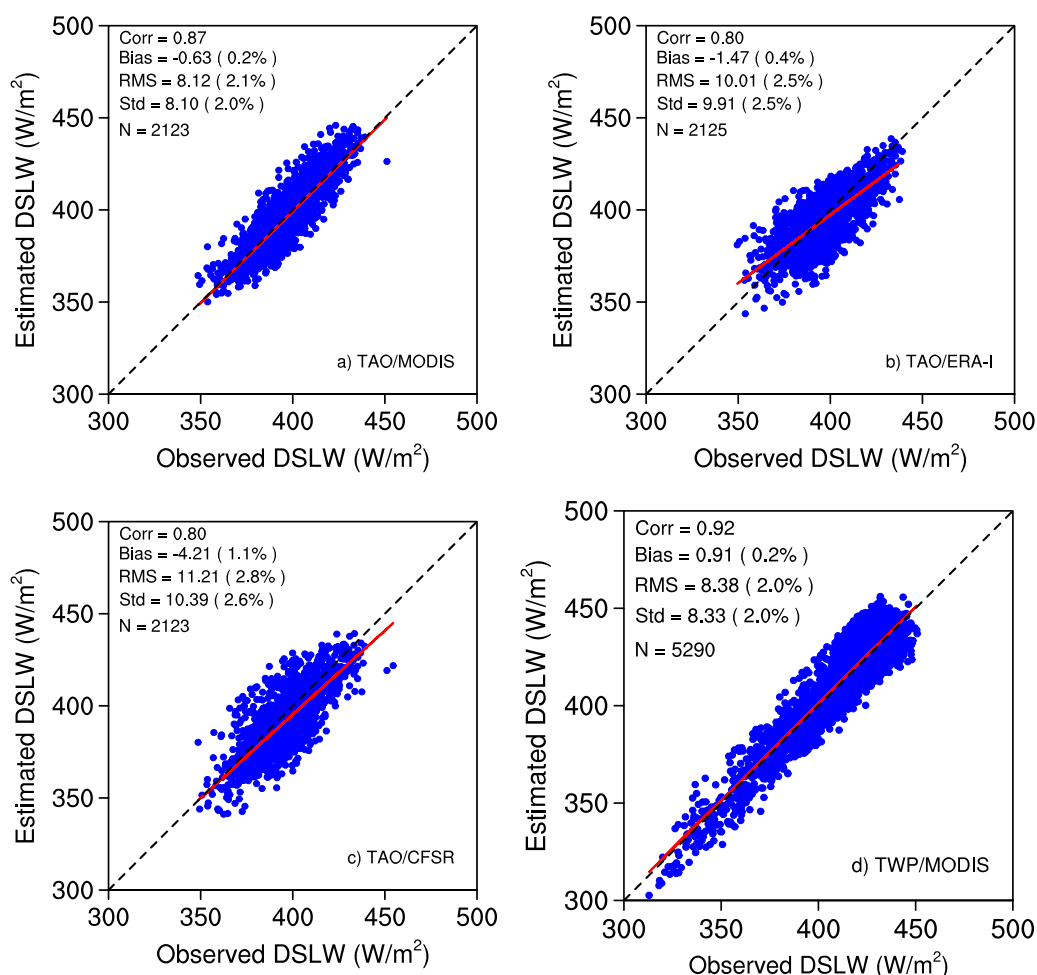


Figure 4. Evaluation of daily downward LW_d fluxes against two TAO buoy sites (0°N, 110°W and 0°N, 125°W) for the period of 2006–2010: (a) UMD/MODIS, (b) ERA-I, (c) CFSR. Buoy observations come from the Tropical Atmosphere Ocean/Triangle Trans-Ocean Buoy Network (TAO/TRITON) moorings in the tropical Pacific Ocean [McPhaden et al., 1998]; (d) evaluation of daily (2006–2010) mean downward LW_d fluxes from UMD_MODIS at three Tropical Western Pacific (TWP) sites (combined) (Manus, Papua New Guinea: 2°3′39.64″S, 147°25′31.43″E; Nauru Island: 0°31′15.6″S, 166°54′57.60″E; and Darwin, Australia: 12°25′28.56″S, 130°53′29.75″E).

Table 5. Assessment of Turbulent Flux Accuracy^a

Statistical Parameters	Product	W10	Qa	SST	Ta	LHF	SHF
Bias	IFREMER	-0.17	-0.07	0.06	-0.19	2.02	1.97
	OAFLux	0.13	-0.70	0.02	-0.20	14.71	0.92
	SEAFLUX	0.14	-0.64	-0.10	-0.37	19.96	0.68
	ERA-I	0.62	-0.29	0.04	-0.05	-2.69	-0.46
	CFSR	0.31	-0.22	0.00	-0.33	-5.89	2.76
Standard deviation	IFREMER	1.12	1.05	0.42	0.63	31.19	6.91
	OAFLux	0.88	1.18	0.41	0.54	32.19	5.17
	SEAFLUX	0.88	1.32	0.43	0.78	40.35	7.84
	ERA-I	1.10	0.75	0.43	0.50	28.33	5.48
	CFSR	1.20	0.83	0.37	0.63	28.73	5.54
Correlation	IFREMER	0.85	0.87	0.98	0.96	0.83	0.81
	OAFLux	0.90	0.89	0.98	0.94	0.83	0.81
	SEAFLUX	0.90	0.86	0.98	0.93	0.78	0.63
	ERA-I	0.89	0.94	0.97	0.96	0.85	0.79
	CFSR	0.84	0.91	0.98	0.96	0.85	0.83

^aTurbulent fluxes are daily averaged data from IFREMER, SeaFlux, OAFLux, ERA Interim, and CFSR. They are compared to daily estimates based on the Tropical Atmosphere Ocean/Triangle Trans-Ocean Buoy Network (TAO/TRITON) data; 17 TAO/TRITON buoys located between 120°W and 80°W, and between 12°N and 10°S are used.

turbulent fluxes are summarized in Table 5. They are based on collocated data occurring when all products are available during the period 2000–2007. They are provided for bulk variables (U_{10} , Qa_{10} , SST, Ta_{10}) as well as for LHF and SHF. As seen, buoy and model estimates compare well. The correlation coefficient between the daily buoy observations and product estimates exceeds 0.80 for all buoys except for few locations. For instance, at 5°N, 95°W the LHF correlation drops to about 0.59 for IFREMER; at 0°N, 95°W the correlation drops to about 0.66 for IFREMER and OAFLux and to 0.49 for SeaFlux (individual cases not shown in Table 5). The poorer results for IFREMER are related to the departures between buoy and IFREMER specific humidity values occurring during certain time periods. Excluding the specific periods associated with high discrepancy between buoy and product Qa leads to an improvement of the correlation between the LHF and SHF to exceed 0.80 (Table 5). This table also indicates that LHF tends to be underestimated compared to buoy estimates (bias of 2.02 W/m²). The highest LHF biases are found for OAFLux (14.71 W/m²) and SeaFlux (19.96 W/m²) due to the specific air humidity Qa bias. Links between LHF biases and the associated bulk variable biases are not straightforward. For instance, ERA-I U_{10} and Qa biases are quite higher than those related to CFSR, but LHF bias is lower for ERA-I. SHF biases are smaller than those for LHF, generally lower than 3 W/m² (SHF values are smaller over tropical oceans as compared to LHF). The standard deviations (*std*) of LHF from buoy estimates and from the various products range between 28.00 and 32.00 W/m². They are highly related to *std* values found for Qa differences. This is consistent with results previously shown, namely, that the accuracy of LHF is highly related to the accuracy of the specific air humidity in tropical area [Bentamy *et al.*, 2013]. While all LHF and SHF products are highly correlated to buoy daily estimates, yet, they are lower than those obtained from the bulk variables. Furthermore, correlation estimated for SHF tends to be lower than LHF correlations. This is mainly related to the correlation between sea and air temperature differences from buoy and from products (not shown).

5. Spatial Variability of Fluxes

5.1. Spatial Variability of Radiative Fluxes

An example of SW_{\downarrow} and LW_{\downarrow} fluxes at the surface as derived from UMD_ISCCP DX at 0.5° resolution for daily mean 15 January 2009 (S. Hemisphere Summer) and 15 July 2009 (S. Hemisphere winter) are shown in Figure 5. Used are the UMD_ISCCP DX data since they are at 0.5° spatial resolution allowing for more detail than the MODIS data (1° spatial resolution). Strong seasonal variability is seen in these examples. At daily time scale, the mean regional SW_{\downarrow} value for January 2009 is 267.98 W/m² while for July 2009 it is between 154.9 W/m². At monthly time scale (figure not shown), the corresponding values for January are between 273.07 W/m² and for July the values are 170.14 W/m². For LW_{\downarrow} fluxes the mean daily value for January 2009 is 380.2 W/m² while for July 2009 it is 363.73 W/m². At monthly time scale (not shown), the corresponding values for January are 378.79 W/m² while for July they are 365.54 W/m². A detailed statistics is presented in

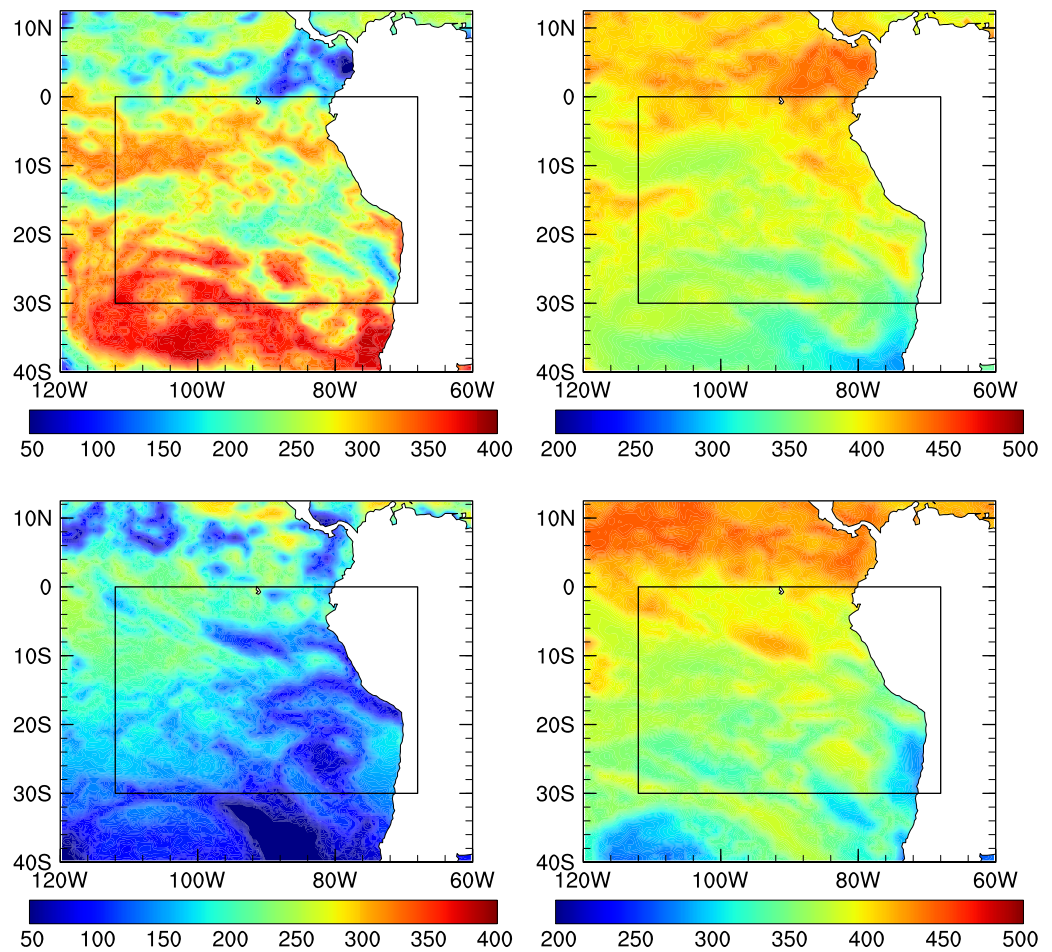


Figure 5. Sample of (left) SW_{\downarrow} fluxes and (right) LW_{\downarrow} at the surface as derived from UMD_ISCCP DX at 0.5° resolution for daily mean (upper) 15 January 2009 and (lower) 15 July 2009.

Table 6. The net radiative fluxes (SW_{\downarrow} and LW_{\downarrow}) as derived from UMD_ISCCP DX at 0.5° resolution for monthly mean January and July 2009 are presented in Figure 6. For the January 2009 case, monthly mean net radiative fluxes show a min of 126.12 W/m^2 and a maximum of 254.43 W/m^2 with a mean value for the Cold Tongue region of 224.82 W/m^2 . For the July 2009 case, monthly mean net radiative fluxes show a min of 40.06 W/m^2 and a maximum of 207.15 W/m^2 with a mean value for the Cold Tongue region of 117.26 W/m^2 . More detailed statistic for the designated region is presented in Table 6 (includes results on turbulent fluxes).

5.2. Spatial Variability of Turbulent Fluxes

Initially, latent and sensible heat flux variabilities over the study area are based on individual buoy estimates of daily values of LHF and SHF fluxes for the period 2000–2009. These results (not shown) are used as a guideline for the analysis of the IFREMER LHF and SHF spatial variabilities. They indicate that the lowest mean LHF values are found along the equator and at the two buoy locations (2°S , 110°W) and (2°S , 95°W) where the lowest SSTs are observed. They do not exceed 60 W/m^2 , while the mean LHF value estimated over the study area is about 100 W/m^2 , and even reaches 150 W/m^2 at locations along 8°S and 5°N . The associated LHF standard deviations indicate that they account for about 50% of mean values of the buoy estimates providing minimum mean LHF values along the equator, at 2°S , 110°W and at 2°S , 95°W , and for about 30% at the rest of buoy locations. The spatial variability of the buoy LHF is also investigated for the 2000–2009 period. As expected, the minimum and maximum values of heat fluxes occur in the northern hemisphere (NH) winter and summer, respectively. For instance, for buoys located along 110°W and 95°W between 2°S and 2°N , there is a factor of 2 between LHF occurring on January (about 50 W/m^2) and July

Table 6. Statistical Information on Radiative and Turbulent Fluxes (W/m^2) in Study Area and at: $95^\circ W$ $2^\circ N$ and $110^\circ W$, $0^\circ N$

Parameter		Daily (2009)		Monthly (2009)		$95^\circ W$, $2^\circ N$	$110^\circ W$, $0^\circ N$
		Jan/15	July/15	Jan	July		
SW ↓	min	70.14	61.97	123.4	93.35		
	max	414.98	248.82	390.62	252.96		
	mean	267.98	154.90	273.07	170.14	225.96	265.10
LW ↓	min	206.64	177.10	218.07	176.16		
	max	435.30	430.0	427.96	418.87		
	mean	380.20	363.73	378.79	365.54	412.955	394.03
LH	min	-11.40	3.40	-5.19	0.66		
	max	292.80	306.80	246.22	265.79		
	mean	98.94	129.47	95.52	130.31	-86.46	-62.53
SH	min	-98.70	-17.80	-35.03	-40.16		
	max	34.30	46.10	23.21	40.75		
	mean	8.20	18.50	9.89	20.67	-11.72	-0.09

(about $100 W/m^2$). However, one should note that the spatial distributions of LHF estimated for January and July are quite similar. The spatial variability of LHF derived from buoys depends on the variability of differences between specific surface and air humidities ($\Delta Q = Q_s - Q_a$) and of surface wind speed (U_{10}). However, at locations where LHF exhibits low mean values ($2^\circ S - 2^\circ N$), the dependency of LHF on ΔQ tends to be higher. Indeed, the correlation between LHF and ΔQ exceed 0.82, whereas LHF and U_{10} correlation is lower than 0.68. Both correlations are significant at 95% confidence level.

The mean values of SHF estimated at each location from daily buoy observations available for the period 2000–2009, do not exceed $10 W/m^2$ except for buoys located along longitude $90^\circ W$ and between $2^\circ N$ and $5^\circ N$ latitudes where they are about $14 W/m^2$. The associated standard deviations are lower than 5 and $10 W/m^2$, respectively.

Figure 7 shows examples of time series of monthly averaged LHF and SHF derived from daily buoy, IFREMER, OAFflux, and SeaFlux estimates. They are calculated for the period January 2000–December 2009 and are shown at six buoy locations between $2^\circ S$ and $2^\circ N$, three along $110^\circ W$ (left column) and three along $95^\circ W$ (right column). Despite several interruptions in buoy time series, the comparison results indicate that the above three flux products tend to track well the in situ data. In particular, the spatial and temporal variabilities derived from IFREMER, OAFflux, and SeaFlux meet those computed from buoys. The correlation coefficient between monthly buoy and estimated LHF and SHF data exceeds 0.80 for all buoys except at $0^\circ N$, $95^\circ W$ where it drops to about 0.66 for IFREMER and OAFflux and 0.49 for SeaFlux. This lower agreement between the $0^\circ N$, $95^\circ W$ buoy and the other estimates relies on significant departure between LHF occurring on October 2002 and October 2003 when LHF from buoy exhibit high values. It was found that these

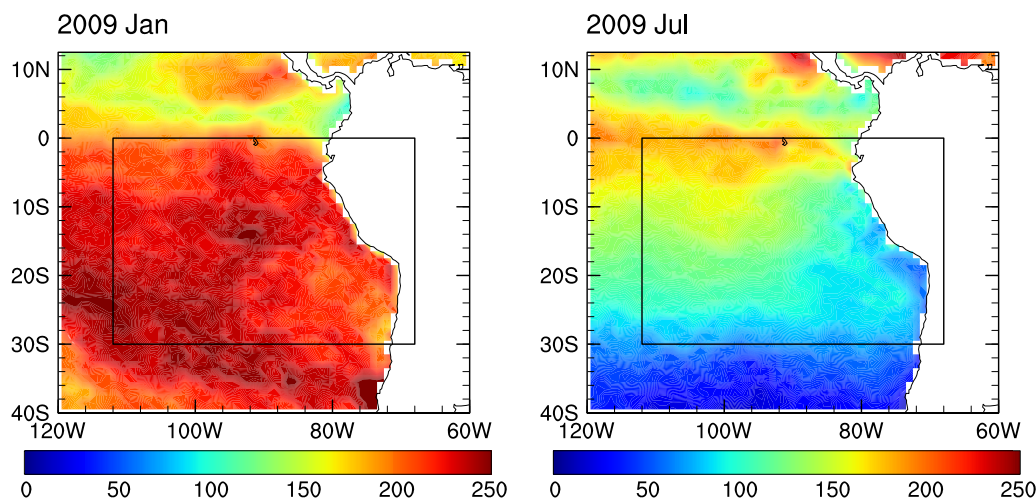


Figure 6. Sample of net radiative fluxes at the surface as derived from UMD_ISCCP DX at 0.5° resolution for monthly mean January and July 2009.

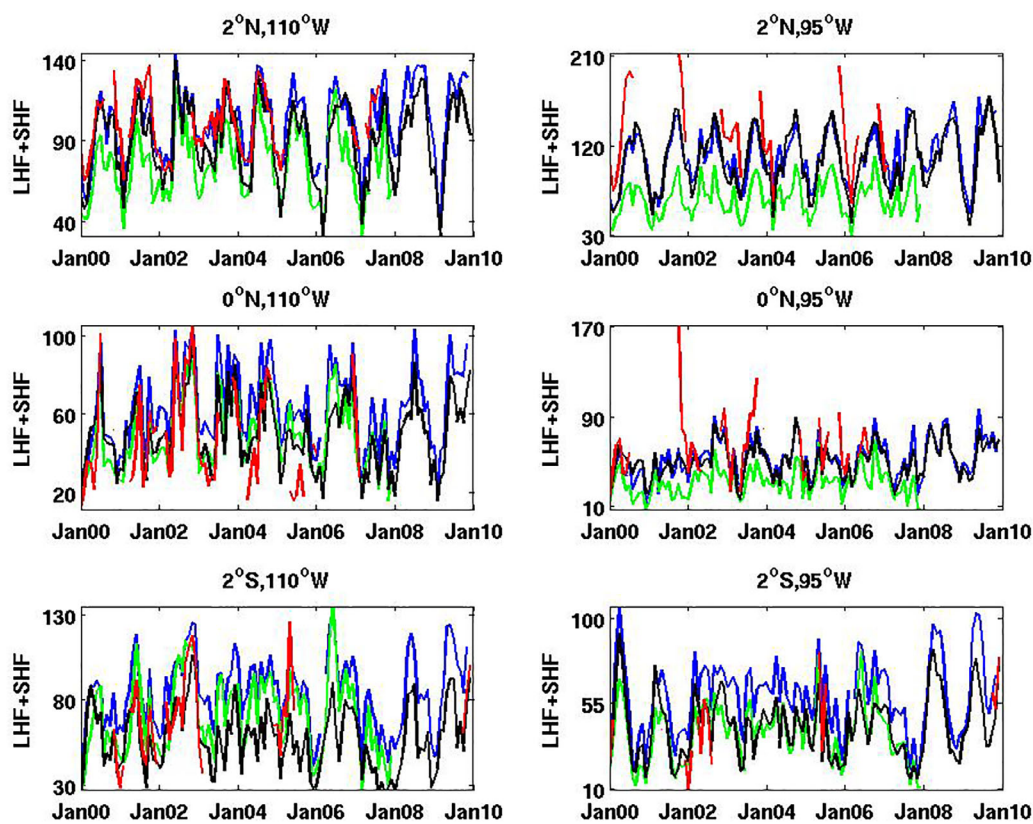


Figure 7. Time series of monthly averaged latent heat fluxes (W/m^2) estimated from daily buoy (red color), IFREMER (blue), OAF flux (black), and SeaFlux (green) for the period 2000–2009. They are shown at buoy locations which coordinates are provided in plot titles.

differences between buoy and the various products are highly related to differences in specific humidity. We found that the difference found at $0^\circ, 95^\circ\text{W}$ in specific air humidity and thus in LHF are mainly due to difference in sampling lengths used for the calculation of buoy and satellite monthly LHF and SHF. For instance, no daily buoy data are available from 1 October to 18 October 2002. Therefore, monthly buoy data estimated for October 2002 are calculated from daily valid data occurring during 19–31 October 2002, whereas IFREMER, OAF flux, and SEAFLUX monthly data are estimated from daily data occurring throughout October 2002 (31 days). Similar explanation holds for October 2003. Excluding these specific months, leads to an improvement of the correlation between the two kinds of heat fluxes which exceeds 0.80.

Further investigations of the LHF and SHF spatial and temporal variabilities are performed over the whole study area based on the use of IFREMER product. Figure 8 show monthly mean estimated for January and July 2009. Strong seasonal variabilities are drawn from these examples for LHF as well as for SHF. The regional averaged LHF and SHF means calculated for January 2009 are about 100.00 and 6.00 W/m^2 , respectively. They both increase to 126.00 and 12.00 W/m^2 for July 2009, which is in good agreement with buoy findings. Some specific zones exhibit much higher seasonal variability. For instance, monthly averaged LHF (SHF) calculated over the zone located within 20°S and 5°S are about 119.00 W/m^2 (6.00 W/m^2) for January and 159.00 W/m^2 (18.00 W/m^2) for July. Along the equatorial Cold Tongue zone monthly averaged LHF increases by a factor of 84% from 50.00 to 92.00 W/m^2 . The spatial distribution of LHF and SHF leads to a significant spatial variability at daily and monthly scales. The highest LHF values are mainly found north 5°N and between 20°S and 5°S , whereas the lowest LHF values are depicted along the equatorial zone. Although, SHF is quite low compared to LHF, it exhibits spatial variability with highest and lowest values mainly located along 5°N and between 15°S and equator, respectively. The origin of such spatial and temporal variabilities of LHF and SHF is highly related to the variability of surface wind speed (W_{10}), specific surface, and air humidity difference ΔQ , and to surface and near air temperature differences ΔT ($\text{SST} - T_a$). For instance LHF pattern found for January 2009 along the equatorial cold tongue (Figure 8) is due to low wind speeds (ranging between 1 and 3 m/s) and low ΔQ differences (ranging between 1.5 and 2.5 g/kg). The

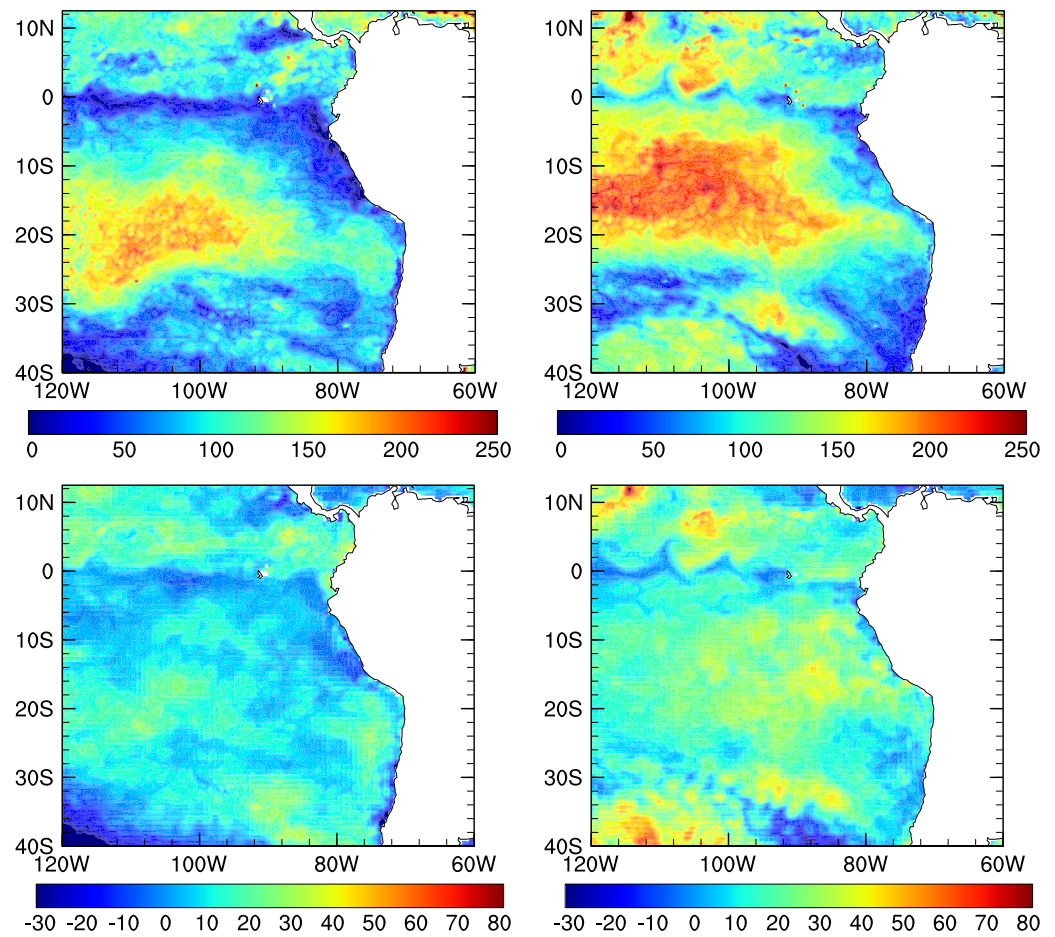


Figure 8. (upper) Mean latent and (lower) sensible fluxes as derived at IFREMER for: (left) 15 January 2009 and (right) 15 July 2009.

investigation of ΔQ difference indicates that low values found along the equator are mainly due to Q_s which is related to sea surface temperature. The latter is a minimum along the equator (not shown). Furthermore, the low wind speed along the equator would result from sea surface temperature and surface wind feedback. Indeed, previous studies showed that atmosphere cooling over cold water increases the stratification of the air column, stabilize the atmospheric marine boundary layer, and thus decrease both vertical turbulent mixing and convection [e. g., Desbiolles *et al.*, 2014].

5.3. Interannual Variability and Mean Annual Cycle of Fluxes

Mean values of net fluxes (radiative and turbulent) are shown in Figure 9 for January 2009 and July 2009. For January 2009, the minimum in net radiative and turbulent flux is 50.19 W/m^2 , the maximum is 214.81 W/m^2 while the mean value is 127.43 W/m^2 . For July 2009, the minimum in net radiative and turbulent flux is 142.95 W/m^2 , the maximum is 181.37 W/m^2 while the mean value is -6.15 W/m^2 .

Two locations have been selected to illustrate the interannual variability of the various fluxes (radiative and turbulent) in the Cold Tongue region for the period of 2003–2010. They are 95°W , 2°N and 110°W and 0° equator (Figure 10). As seen, the interannual variability in the air-sea latent heat flux in the cold-tongue region is dominated by the variability in net shortwave radiation, and as such, the net $\text{SW}\downarrow$ flux dominates the total net flux in this region. Due to equatorial proximity, the amplitude of the $\text{SW}\downarrow$ fluxes is relatively small, around 50 W/m^2 at northern site and much smaller at the equator. The mean values over the 7 year period are about 226.00 and 265.00 W/m^2 , respectively. The mean $\text{LW}\downarrow$ flux is about 413.00 and 349.00 W/m^2 , respectively, while the $\text{LW}\downarrow$ interannual variability is negligible; the net $\text{LW}\downarrow$ changes between about -31.00 to -41.00 W/m^2 , respectively. The latent and sensible heat fluxes are negative about -86.00 and

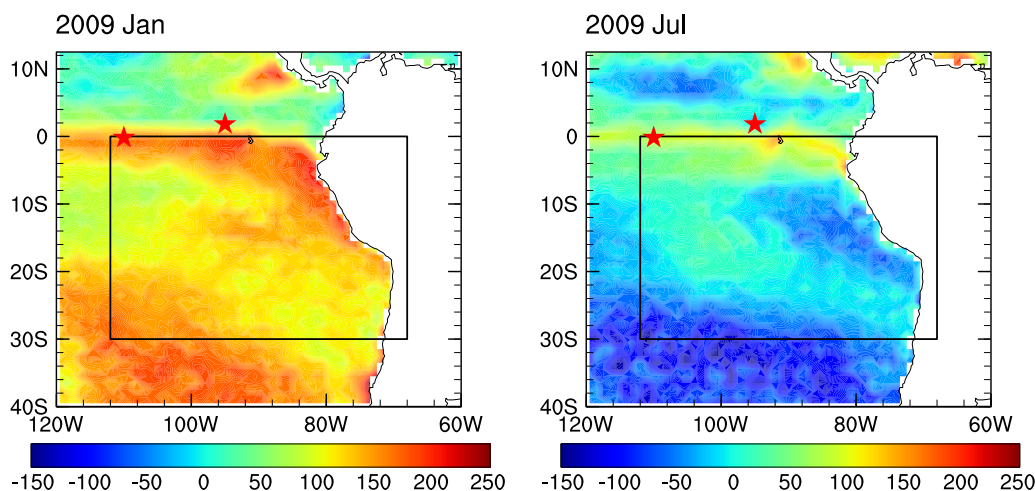


Figure 9. Monthly mean net fluxes (radiative and turbulent) for (left) January 2009 and (right) July 2009.

−62.00 W/m², respectively, while the total net flux (turbulent and radiative) is 84.00 and 143 W/m², respectively (Table 6).

The annual cycle for the two selected locations (95°W, 2°N and 110°W and 0° equator) is shown in Figure 11. It represents average values for about 7 years; as evident, except for the SW↓ and LHF fluxes the variability is negligible.

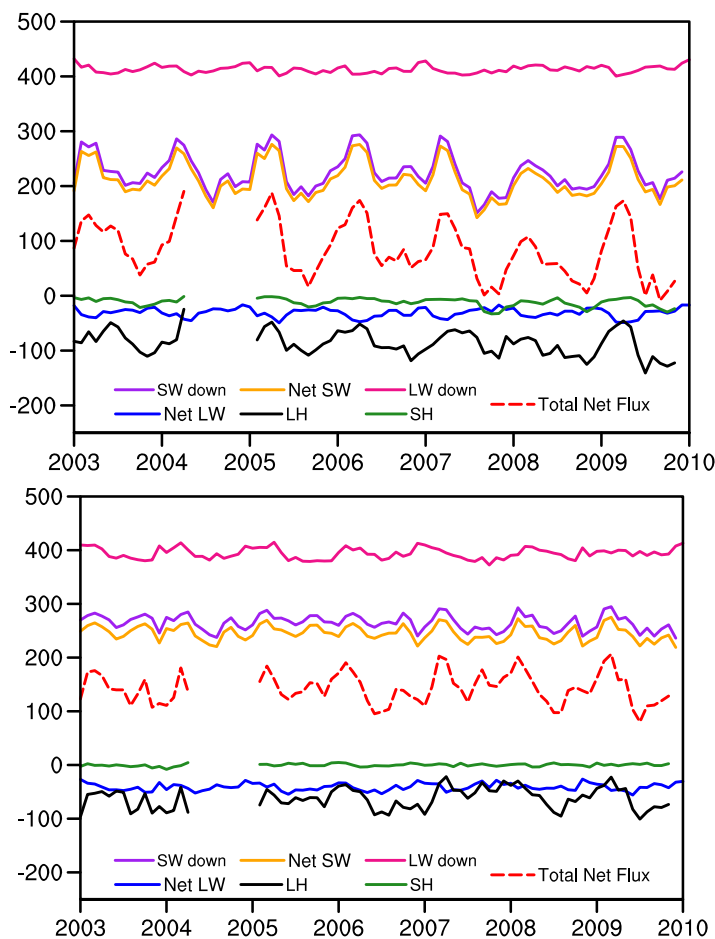


Figure 10. Time series of radiative and turbulent fluxes in W/m² at: above: 95°W, 2°N; below: 110°W, 0°N.

6. Discussion and Summary

The complexity of the cloud fields in the Cold Tongue regions has been discussed by numerous investigators. Studies that focused on the spatial and temporal variabilities of clouds, identified mesoscale subgrid scale structures such as pockets of open cells [Stevens *et al.*, 2005] that are embedded in uniform stratocumulus. Wood and Hartmann [2006] found that mesoscale convective complexes (MCCs) are strongly associated with the spatial variability of liquid water path (LWP) and CF in the marine stratocumulus regions off the Californian and Peruvian coasts. Jensen *et al.* [2008] used a set of multiyear observations and found that while MBL clouds are often considered plane parallel, overcast clouds occur in only about 25% of the scenes. These findings have an implication for the accuracy at which satellite SW↓

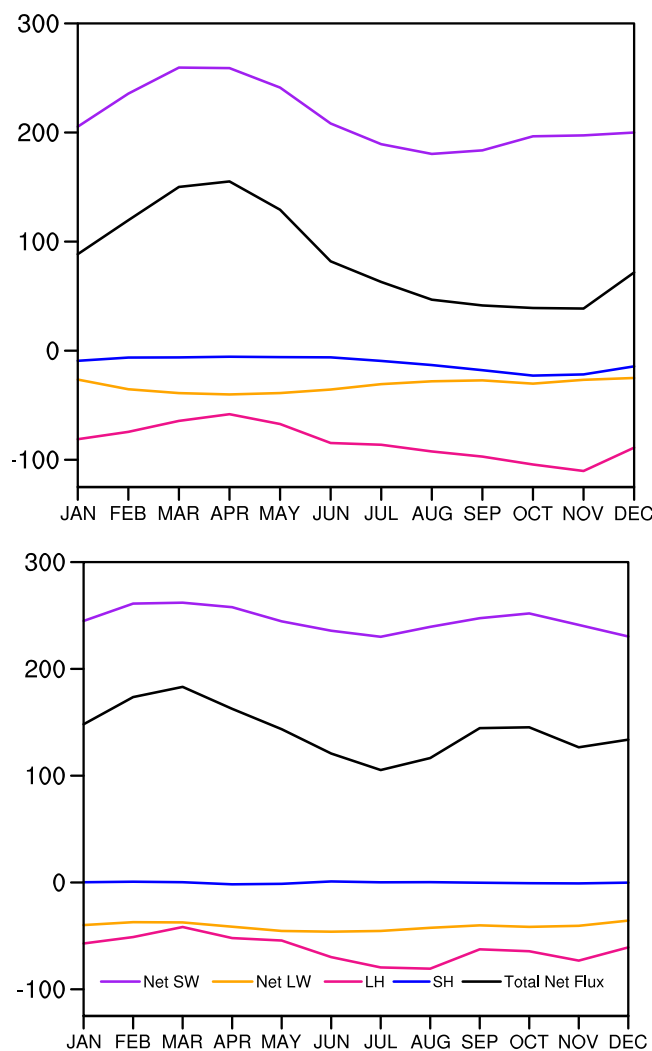


Figure 11. Annual cycle of radiative and turbulent fluxes in W/m^2 at: above: $95^\circ W, 2^\circ N$; below: $110^\circ W, 0^\circ N$.

spatial and temporal variabilities of both the LHF and the SHF. The standard deviations associated with their mean values may reach 50%.

This study represents an effort to evaluate established satellite and numerical model capabilities to provide information on net fluxes (turbulent and radiative) at the complex Cold Tongue region, at spatial and temporal scales of interest in climate applications. Using state-of-the-art observations and models, we have provided statistics and patterns of the net heat budget across the surface/atmosphere interface and evaluated how accurately components of this budget can be estimated in an area of climatic significance where models encounter difficulties. We have confirmed that the net heat flux is dominated by the $SW\downarrow$ radiation which also controls the latent heat flux [Pinker et al., 2014]. The SHF flux term is relatively small, so biases in its magnitude will not dominate the budget. While observations of $SW\downarrow$ fluxes from buoys in that region are relatively numerous, there are no sufficient measurements of $LW\downarrow$ to robustly evaluate corresponding satellite-based estimates. We have also illustrated the intrinsic difficulties in the process of evaluation; statistical results do depend on the number of sites selected for evaluation, and differences in the quality of the observations from site to site. With progress made in quality and density of ground observation and satellite observations that can now resolve the vertical structure of clouds, such as the A-train configuration, it would be possible to determine to what extent satellite estimates of radiative fluxes can be improved in that region. It was clearly shown that the satellite estimates of radiative fluxes are in much closer agreement with ground observations than those from numerical models. It was also shown that in the Tropical Pacific

radiative fluxes can be estimated, in particular, since most inference schemes assumes the “plane parallel approximation” that does not depict correctly complex structures; moreover, there is no direct observational information on the cloud base height which impacts the accuracy of the $LW\downarrow$ fluxes. However, as yet, information on detailed characterization of clouds in this regions is not readily available for routine estimates of radiative fluxes from satellite observations; as such there is a need to establish how well current methodologies can estimate such fluxes from available and consistent long-term information. It was found that for the satellite-based estimates the standard deviations for $SW\downarrow$ were in the range of 7.2–7.8% of the mean and in the range of 2.0–2.5% for $LW\downarrow$, at daily time scale. For $SW\downarrow$ fluxes, the range of standard deviation in the models was 11.5–17.2% from the mean while for the $LW\downarrow$ fluxes it was in the range of 2.5–2.6%, in close agreement with satellite methods. This can be expected since $SW\downarrow$ fluxes are primarily controlled by clouds while for $LW\downarrow$ fluxes water vapor also plays an important role. In the tropics where water vapor levels are high, their effect on the $LW\downarrow$ is dominant and, as such, should reduce its variability [Hall and Manabe, 2000]. The assessment of turbulent heat fluxes indicate high

regions outside the PCT, estimates of LHF and SHF from numerical models are in very close agreement with the satellite methods indicating the powerful impact from assimilation of buoy observations in these models.

Appendix A

Supplementary information on section 2.1(1) is provided here. The ISCCP DX data are stored satellite by satellite. There are five geostationary satellites (4 before 1998) and two polar orbiting satellites that provide input to the ISCCP DX data base. Ideally, five geostationary satellites should be available simultaneously for a global coverage up to about 55°N and 55°S. Before July 1998 only 3–4 geostationary satellites were available. Meteosat-5 has been moved over the Indian Ocean only in 1998 to remove a geostationary gap over that region. We compute the radiative fluxes for each satellite domain independently. The quality of the computed radiative fluxes is not equal within the geostationary domain; the outer pixels with a larger viewing zenith angle cover larger footprints and tend to impact the estimated radiative fluxes. There is a need for a merging scheme to combine information from the multisources to produce complete and homogeneous information on radiative fluxes at global scale. For geostationary satellites, the merging scheme uses the monthly mean cosine of the satellite view angle as a weighting factor to obtain a weighted average from various satellites. Fluxes from polar orbiting satellite are assigned a fixed weighting factor; values depend on the latitude of the grid point. At lower latitudes, fluxes are a weighted average as derived from geostationary satellites. In the gap regions between geostationary satellites, missing values are filled with observations from polar orbiting satellite. In this study, we are interested in radiative fluxes which are hemispherical integral quantities and as such, it is possible to average them even if they come from two different satellites (e.g., in areas of overlap between satellites). The scheme we use is a combination of the scheme used when producing the ISCCP D1 of satellite observations [Zhang *et al.*, 2004], and one developed for this study. Specifically, in the GISS version of the ISCCP D1 scheme, for every location, a hierarchy of preferred satellite observation is specified. At any time, only one satellite is selected for each location. In our scheme, for every location, all available observations are used to create the merged product.

Appendix B: Homogenization of the Independent Satellite Data Used

Evaluation of the ISCCP-DX data over oceans [Ma and Pinker, 2012] shows that the satellite retrievals tend to overestimate the $SW\downarrow$ over oceans, in particular, over the Atlantic (not the case over land). Evaluation of $SW\downarrow$ fluxes as derived from the Moderate Resolution Imaging Spectroradiometer (MODIS) observations shows better agreement between the estimates and the observations against buoy observations as compared to the ISCCP-DX estimates [Pinker *et al.*, 2009]. It was opted to adjust the biases in the ISCCP-DX fluxes based on the MODIS observations. The mean bias of $SW\downarrow$ for ISCCP DX relative to MODIS was derived from the mean differences from August 2002 to December 2009. The mean values for ISCCP DX and MODIS are 191.77 and 183.82 W/m^2 , respectively, with the difference as 7.95 W/m^2 at global scale. To make correction to daily fluxes, the bias was normalized by top of atmosphere daily shortwave down flux. The resulting data sets (after bias removal) and removal of the annual mean cycle (to be described in the next section) are being used in this study. The same was done for the $LW\downarrow$ fluxes; however, the differences between the two data sets were not as large as in the case of $SW\downarrow$ fluxes.

Appendix C: Accuracy of Ground Observations

Additional issues that impact the estimation of accuracy at which the surface fluxes can be determined is related to the ground observations. There are several ways that the analysis may be improved. The $SW\downarrow$ radiative flux consists of both a direct component of radiation from the sun and a diffuse component of scattered sunlight from the sky. The global radiation can be measured directly by a pyranometer or as a sum of the direct and diffuse component which is considered as a better way to get the total flux [Long *et al.*, 2010]. Such information is not readily available, and nonexistent at buoy sites (it is available at the BSRN sites but not as readily as the total global value). Significant offsets can occur in $SW\downarrow$ measurements made from moving platforms due to the tilt of the instruments from horizontal, which changes the angular orientation of the direct component of sunlight to the instrument and causes an artificial variation in the measured signal. As discussed by Long *et al.* [2010], to properly correct for this tilt, a priori knowledge of the

partitioning between the direct and diffuse components of the total shortwave irradiance is needed to properly apply a correction for tilt. This partitioning information can be adequately provided using a newly available commercial radiometer named the SPN1 that produces reasonable measurements of the total and diffuse shortwave irradiance (and by subtraction of the direct shortwave irradiance) with no moving parts and regardless of azimuthal orientation. Using data from the recent RACORO campaign, methodologies were developed for determining the constant pitch and roll offsets of the radiometers for applying a tilt correction to the total shortwave irradiance data. Results suggest that the methodology is accurate for tilt up to $\pm 10^\circ$, with 90% of the data corrected to within 10 W/m^2 at least for clear-sky data. Without a proper tilt correction, even data limited to 5° of tilt can still exhibit large errors, greater than 100 W/m^2 in some cases. For the TRITON/TAO array, downwelling SW \downarrow is detected by the Eppley Laboratory pyranometers that have nominal resolution 0.4 W/m^2 and relative accuracy of $\pm 2\%$ in the $0\text{--}1600 \text{ W/m}^2$ interval in laboratory conditions [Cronin and McPhaden, 1997].

Acknowledgments

The analysis was completed under NASA grant NNX13AC12G, the Energy and Water Cycle Study (NEWS) program. The work benefited from support under NASA grant NNX08AN40A from the Science Mission Directorate-Division of Earth Science. Thanks are due to the NASA GES DISC Giovanni for the MODIS data, to the various MODIS teams that produced data used in this study, and to the NASA Langley Research Center Atmospheric Science Data Center for providing the ISCCP DX data. We acknowledge the TAO Project Office of NOAA/PMEL for providing data from the Tropical Atmosphere Ocean/Triangle Trans-Ocean Buoy Network (TAO/TRITON) that were used in this study and the Tropical Western Pacific Office (TWPO) at Los Alamos National Laboratory for operating the Tropical Western Pacific (TWP) sites. A. Bentamy wishes to thank S. Grodsky, University of Maryland (USA), A. Mestas-Núñez, University of Corpus Christi (USA), B. Blanke, University of Bretagne Ouest (UBO/France), and F. Desbiolles, IFREMER/LOS (France) and UBO, for their comments, suggestions, and encouragement that led to improvement in turbulent flux estimates derived from remotely sensed data. He also thanks F. Paul, D. Croize-Fillon, J.F. Piolle, and IFREMER/CERSAT for data processing support and is grateful to ECMWF, EUMETSAT, CERSAT, JPL, ISRO, NOAA, NOCS, Meteo-France, NDBC, PMEL, and UK MetOffice for providing numerical, satellite, and in situ data. The Ocean Heat flux data can be downloaded from the dedicated portal <http://oceanflux.cersat.fr/>. The radiative fluxes will be provided upon request from the corresponding author. We are grateful to two anonymous reviewers for very helpful and constructive comments and to the Editor for overseeing the disposition of this manuscript.

References

Atlas, R., R. N. Hoffman, J. Ardizzone, S. M. Leidner, J. C. Jusem, D. K. Smith, and D. Gombos (2011), A cross-calibrated, multiplatform ocean surface wind velocity product for meteorological and oceanographic applications, *Bull. Am. Meteorol. Soc.*, *92*, 157–174.

Bentamy, A., and D. Croize-Fillon (2014), Spatial and temporal characteristics of wind and wind power off the coasts of Brittany, *Renew. Energy*, *66*, 670–679.

Bentamy, A., S. A. Grodsky, K. Katsaros, A. M. Mestas-Nunez, B. Blanke, and F. Desbiolles (2013), Improvement in air-sea flux estimates derived from satellite observations, *Int. J. Remote Sens.*, *34*(14), 5243–5256.

Berrisford, P., D. Dee, K. Fielding, M. Fuentes, P. Källberg, S. Kobayashi, and S. Uppala (2009), The ERA-Interim archive, version 1.0, *ERA Rep. Ser. 1*, Eur. Cent. for Medium-Range Weather Forecasts, Reading, U. K.

Chou, S.-H., R. Atlas, C.-L. Shie, and J. Ardizzone (1995), Estimates of surface humidity and latent heat fluxes over oceans from SSM/I data, *Mon. Weather Rev.*, *123*, 2405–2425, doi:10.1175/1520-0493(1995)123<2405:EOSHAL>2.0.CO;2.

Chou, S.-H., C.-L. Shie, R. M. Atlas, and J. Ardizzone (1997), Air-sea fluxes retrieved from Special Sensor Microwave Imager data, *J. Geophys. Res.*, *102*, 12,706–12,726.

Clayson, C. A., J. B. Roberts, and A. Bogdanoff (2013), The effect of diurnal sea surface temperature warming on climatological air-sea fluxes, *J. Clim.*, *26*, 2546–2556.

Cronin, M. F., and M. J. McPhaden (1997), The upper ocean heat balance in the western equatorial Pacific warm pool during September–December 1992, *J. Geophys. Res.*, *102*, 8533–8553.

Dee, D. P., M. Balmaseda, G. Balsamo, R. Engelen, A. J. Simmons, and J. N. Thépaut (2013), Toward a consistent reanalysis of the climate system, *Bull. Am. Meteorol. Soc.*, *95*(8), 1235–1248, doi:10.1175/bams-d-13-00043.1.

Desbiolles, F., B. Blanke, A. Bentamy, and N. Grima (2014), Origin of fine-scale wind stress curl structures in the Benguela and Canary Upwelling systems, *J. Geophys. Res. Oceans*, *119*, 7931–7948, doi:10.1002/2013JC009278.

Fairall, C. W., E. F. Bradley, J. E. Hare, A. A. Grachev, and J. B. Edson (2003), Bulk parameterization of air-sea fluxes: Updates and verification for the COARE algorithm, *J. Clim.*, *16*(4), 571–591.

Fore, A. G., B. W. Stiles, A. H. Chau, B. Williams, R. S. Dunbar, and E. Rodriguez (2014), Pointwise wind retrieval and ambiguity removal improvements for the QuikSCAT climatological data set, *IEEE Trans. Geosci. Remote Sens.*, *52*(1), 51–59.

Hall, A., and S. Manabe (2000), Effect of water vapor feedback on internal and anthropogenic variations of the global hydrologic cycle, *J. Geophys. Res.*, *105*, 6935–6944.

Jensen, E. J., et al. (2008), Formation of large ($\approx 100 \mu\text{m}$) ice crystals near the tropical tropopause, *Atmos. Chem. Phys.*, *8*, 1621–1633, doi:10.5194/acp-8-1621-2008.

Josey, S. A., S. Gulev, and L. Yu (2013), Exchanges through the ocean surface, in *Ocean Circulation and Climate 2nd Ed. A 21st Century Perspective*, vol. 103, Int. Geophys. Ser., edited by G. Siedler et al., pp. 115–140, Academic, San Diego, Calif.

Josey, S. A., L. Yu, S. Gulev, X. Jin, N. Tilinina, B. Barnier, and L. Brodeau (2014), Unexpected impacts of the Tropical Pacific array on reanalysis surface meteorology and heat fluxes, *Geophys. Res. Lett.*, *41*, 6213–6220, doi:10.1002/2014GL061302.

King, M. D., Y. J. Kaufman, W. P. Menzel, and D. Tanré (1992), Remote sensing of cloud, aerosol, and water vapor properties from the Moderate Resolution Imaging Spectrometer (MODIS), *IEEE Trans. Geosci. Remote Sens.*, *30*, 2–27, doi:10.1109/36.124212.

Klein, S. A., and D. L. Hartmann (1993), The seasonal cycle of low stratiform clouds, *J. Clim.*, *6*, 1587–1606.

Kummerow, C., W. Berg, M. Sapiano, N. Rodriguez-Alvarez, and F. Weng (2013), A fundamental climate data record of intercalibrated brightness temperature data from SSM/I and SSMIS, CDR Team Meeting July 30–Aug 1, 2013.

Legler, D. M., and J. J. O'Brien (1985), *Atlas of Tropical Pacific Wind-Stress Climatology 1971–1980*, pp. 187, Florida State Univ., Tallahassee, Fla.

Long, C. N., and S. A. McFarlane (2012), Quantification of the impact of Nauru Island on ARM measurements, *J. Appl. Meteorol. Climatol.*, *51*, 628–636, doi:10.1175/JAMC-D-11-0174.1.

Long, C. N., A. Bucholtz, H. Jonsson, B. Schmid, A. Vogelmann, and J. Wood (2010), A method of correcting for tilt from horizontal in downwelling shortwave irradiance measurements on moving platforms, *The Open. Atmos. Sci. J.*, *4*, 78–87, doi:10.2174/1874282301004010078.

Ma, C.-C., C. R. Mechoso, A. Arakawa, and J. D. Farrara (1994), Sensitivity of a coupled ocean-atmosphere model to physical parameterizations, *J. Clim.*, *7*, 1883–1896.

Ma, Y., and R. T. Pinker (2012), Modeling shortwave radiative fluxes from satellites, *J. Geophys. Res.*, *117*, D23202, doi:10.1029/2012JD018332.

McFarlane, S. A., C. N. Long, and D. M. Flynn (2005), Impact of island-induced clouds on surface measurements: Analysis of the ARM Nauru Island effect study data, *J. Appl. Meteorol.*, *44*, 1045–1065.

McPhaden, M. J., et al. (1998), The tropical ocean-global atmosphere observing system: A decade of progress, *J. Geophys. Res.*, *103*, 14,169–14,240.

Mochizuki, T., T. Miyama, and T. Awaji (2007), A simple diagnostic calculation of marine stratocumulus cloud cover for use in general circulation models, *J. Geophys. Res.*, *112*, D06113, doi:10.1029/2006JD007223.

- Nussbaumer, E. A., and R. T. Pinker (2012), Estimating surface longwave radiative fluxes from satellites utilizing artificial neural networks, *J. Geophys. Res.*, *117*, D07209, doi:10.1029/2011JD017141.
- Oberhuber, J. M. (1988), An Atlas based on the "COADS" Data set the budgets of heat, buoyancy and turbulent kinetic energy the surface of the global ocean, *Max Planck Institute for Meteorology Rep. 15*, Max-Planck-Inst. für Meteorol., Hamburg, Germany.
- Ohmura, A., et al. (1998), Baseline Surface Radiation Network (BSRN/WCRP): New precision radiometry for climate research, *Bull. Am. Meteorol. Soc.*, *79*, 2115–2136.
- Pinker, R. T., H. Wang, and S. A. Grodsky (2009), How good are ocean buoy observations of radiative fluxes?, *Geophys. Res. Lett.*, *36*, L10811, doi:10.1029/2009GL037840.
- Pinker, R. T., A. Bentamy, K. B. Katsaros, Y. Ma, and C. Li (2014), Estimates of net heat fluxes over the Atlantic Ocean, *J. Geophys. Res. Oceans*, *119*, 410–427, doi:10.1002/2013JC009386.
- Reynolds, R. W., T. M. Smith, C. Liu, D. B. Chelton, K. S. Casey, and M. G. Schlax (2007), Daily high-resolution-blended analyses for sea surface temperature, *J. Clim.*, *20*, 5473–5496.
- Ricciardulli, L., and F. Wentz (2011), Reprocessed QuikSCAT (V04) wind vectors with Ku-2011 geophysical model function, *Remote Sens. Syst. Tech. Rep. 043011*, Remote Sensor Syst. (RSS) Co. [Available at http://www.ssmi.com/qscat/qscat_Ku2011_tech_report.pdf.]
- Riihimaki, L. D., and C. N. Long (2014), Spatial variability of surface irradiance measurements at the Manus ARM site, *J. Geophys. Res. Atmos.*, *119*, 5475–5491, doi:10.1002/2013JD021187.
- Roberts, J. B., C. A. Clayson, F. R. Robertson, and D. Jackson (2010), Predicting near-surface characteristics from SSM/I using neural networks with a first guess approach, *J. Geophys. Res.*, *115*, D19113, doi:10.1029/2009JD013099.
- Rossow, W. B., and R. A. Schiffer (1991), ISCCP cloud data products, *Bull. Am. Meteorol. Soc.*, *72*, 2–20, doi:10.1175/1520-0477(1991)072<0002:ICDP>2.0.CO;2.
- Saha, S., et al. (2010), The NCEP climate forecast system reanalysis, *Bull. Am. Meteorol. Soc.*, *91*, 1015–1057, doi:10.1175/2010BAMS3001.1.
- Sapiano, M. R. P., W. K. Berg, D. S. McKague, and C. D. Kummerow (2012), Toward an intercalibrated fundamental climate data record of the SSM/I sensors, *IEEE Trans. Geosci. Remote Sens.*, *51*(3), 1492–1503, doi:10.1109/TGRS.2012.2206601.
- Siebesma, A., et al. (2004), Cloud representation in general circulation models over the northern Pacific Ocean: A EUROCS intercomparison study, *Q. J. R. Meteorol. Soc.*, *130*, 3245–3267.
- Stevens, B., et al. (2005), Evaluation of large-eddy simulations via observations of nocturnal marine stratocumulus, *Mon. Weather Rev.*, *133*, 1443–1462, doi:10.1175/MWR2930.1.
- Swenson, M. S., and D. V. Hansen (1999), Tropical Pacific Ocean Mixed Layer Heat Budget: The Pacific Cold Tongue, *J. Phys. Oceanogr.*, *29*, 69–81.
- Wang, H., and R. T. Pinker (2009), Shortwave radiative fluxes from MODIS: Model development and implementation, *J. Geophys. Res.*, *114*, D20201, doi:10.1029/2008JD010442.
- WCRP (2012), Action Plan for WCRP Research Activities on Surface Fluxes, *WCRP Informal/Ser. Rep. 01*, World Meteorol. Organ. (WMO), doi:10.1175/JCLI-D-14-00591.1.
- WCRP (2013), Report from the World Climate Research Program (WCRP), May 2013. CLIVAR/ESA Scientific Consultation Workshop on: "Earth Observation Measurement Constraints on Ocean Heat Budget", World Meteorol. Organ. (WMO).
- Wentz, F. J. (1997), A well calibrated ocean algorithm for special sensor microwave/imager, *J. Geophys. Res.*, *102*, 8703–8718.
- Wood, R., and D. L. Hartmann (2006), Spatial variability of liquid water path in marine low cloud: The importance of mesoscale cellular convection, *J. Clim.*, *19*, 1748–1764.
- Woodruff, S. D., R. J. Slutz, R. L. Jenny, and P. M. Steurer (1987), A comprehensive ocean-atmosphere data set, *Bull. Am. Meteorol. Soc.*, *68*(10), 1239–1250, doi:10.1175/1520-0477(1987)068<1239:ACOADS>2.0.CO;2.
- Yu, J. Y., and C. R. Mechoso (1999), A discussion on the errors in the surface heat fluxes simulated by a coupled GCM, *J. Clim.*, *12*(2), 416–426.
- Yu, L., X. Jin, and R. A. Weller (2008), Multidecade Global Flux Datasets from the Objectively Analyzed Air-sea Fluxes (OAFux) Project: Latent and sensible heat fluxes, ocean evaporation, and related surface meteorological variables, *Tech. Rep. OAFux Proj. OA2008-01*, Woods Hole Oceanogr. Inst.
- Yu, L., K. Haines, M. Bourassa, S. Gulev, S. Josey, T. Lee, M. Cronin, and A. Kumar (2012), *CLIVAR GSOP WHOI Workshop Report on Ocean Syntheses and Surface Flux Evaluation*, WHO, Woods Hole, Mass.
- Yu, L., K. Haines, M. Bourassa, M. Cronin, S. Gulev, S. Josey, S. Kato, A. Kumar, T. Lee, and D. Roemmich (2013), Towards achieving global closure of ocean heat and freshwater budgets: Recommendations for advancing research in air-sea fluxes through collaborative activities, *International Clivar Project Office, 2013: Int. CLIVAR Publ. Ser. 189*, WHO. [Available at http://www.clivar.org/sites/default/files/ICPO189_WHOI_fluxes_workshop.pdf.]
- Zhang, G. J., A. M. Vogelmann, M. P. Jensen, W. D. Collins, and E. P. Luke (2010), Relating satellite-observed cloud properties from MODIS to meteorological conditions for marine boundary layer clouds, *J. Clim.*, *23*, 1374–1391.
- Zhang, Y., W. B. Rossow, A. A. Lacis, V. Oinas, and M. I. Mishchenko (2004), Calculation of radiative fluxes from the surface to top of atmosphere based on ISCCP and other global data sets: Refinements of the radiative transfer model and the input data, *J. Geophys. Res.*, *109*, D19105, doi:10.1029/2003JD004457.